



**HAL**  
open science

## Microscale ultrahigh-frequency resonant wireless powering for capacitive and resistive MEMS actuators

Yoshio Mita, Naoyuki Sakamoto, Naoto Usami, Antoine Frappé, Akio Higo, Bruno Stefanelli, Hidehisa Shiomi, Julien Bourgeois, Andreas Kaiser

### ► To cite this version:

Yoshio Mita, Naoyuki Sakamoto, Naoto Usami, Antoine Frappé, Akio Higo, et al.. Microscale ultrahigh-frequency resonant wireless powering for capacitive and resistive MEMS actuators. Sensors and Actuators A: Physical , 2018, 275, pp.75-87. 10.1016/j.sna.2018.03.020 . hal-02182815

**HAL Id: hal-02182815**

**<https://hal.science/hal-02182815>**

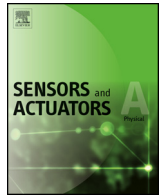
Submitted on 13 Jul 2022

**HAL** is a multi-disciplinary open access archive for the deposit and dissemination of scientific research documents, whether they are published or not. The documents may come from teaching and research institutions in France or abroad, or from public or private research centers.

L'archive ouverte pluridisciplinaire **HAL**, est destinée au dépôt et à la diffusion de documents scientifiques de niveau recherche, publiés ou non, émanant des établissements d'enseignement et de recherche français ou étrangers, des laboratoires publics ou privés.



Distributed under a Creative Commons Attribution 4.0 International License



## Microscale ultrahigh-frequency resonant wireless powering for capacitive and resistive MEMS actuators



Yoshio Mita<sup>a,c,f,\*</sup>, Naoyuki Sakamoto<sup>a</sup>, Naoto Usami<sup>a</sup>, Antoine Frappé<sup>b</sup>, Akio Higo<sup>c</sup>, Bruno Stefanelli<sup>b</sup>, Hidehisa Shiomi<sup>d</sup>, Julien Bourgeois<sup>e</sup>, Andreas Kaiser<sup>b</sup>

<sup>a</sup> Department of Electrical Engineering and Information Systems, Graduate School of Engineering, The University of Tokyo, 7-3-1, Hongo Bunkyo-ku, 113-8656 Tokyo, Japan

<sup>b</sup> IEMN-ISEN, CNRS UMR 8520, 41, Boulevard Vauban, 59046 Lille cedex, France

<sup>c</sup> VLSI Design and Education Center, The University of Tokyo, 2-11-16, Yayoi Bunkyo-ku, 113-8656 Tokyo, Japan

<sup>d</sup> Graduate School of Engineering Science, Osaka University, 1-3, Machikaneyamacho Toyonaka, 560-8531 Osaka, Japan

<sup>e</sup> FEMTO-ST Institute, Univ. Bourgogne Franche-Comté, CNRS, Montbéliard, France

<sup>f</sup> LIMMS, CNRS-UTokyo IIS, UMI 2820, 4-6-1, Komaba Meguro-ku, 153-8505 Tokyo, Japan

### ARTICLE INFO

#### Article history:

Received 4 February 2018

Received in revised form 13 March 2018

Accepted 15 March 2018

Available online 3 April 2018

#### Keywords:

Wireless MEMS powering

Ultrahigh frequency (UHF)

Radio frequency

Resonant mode energy transfer

Electrostatic actuator

Thermal actuator

Amplitude modulation (AM)

### ABSTRACT

This paper presents a versatile chip-level wireless driving method for microelectromechanical system (MEMS) actuators. A MEMS actuator is integrated as an electrical component of a coupled LCR resonant circuit, and it rectifies the energy sent through an ultrahigh-frequency (UHF) radio frequency (RF) wave. Two types of actuators were remotely driven using the proposed method: thermal (bimorph) actuators used as the R component and capacitive (comb-drive) actuators used as the C component of a resonant receiver circuit. We demonstrated the remote actuation of a  $13\ \Omega$  thermal actuator transferring 7.05 mW power with a power efficiency of 15.8%. This was achieved using coupled  $500\ \mu\text{m}$  diameter 5.5-turn planar coil antennas over a distance of  $90\ \mu\text{m}$ . When an impedance-matching configuration ( $Z_0 = 50\ \Omega$ ) was used, the efficiency over a distance of  $65\ \mu\text{m}$  was measured to be 55.6%, which was 8.2 times greater than that of simple inductor coupling. The proposed method can be applied to future deployment scenarios, where fragile MEMS are placed on top of a system and must directly interface with the environment (thus, being prone to break). The authors propose to fabricate MEMS and energy receiver circuits monolithically on a chip, and place them on another energy transmitter chip. Thereby, the MEMS chip can avoid electrical feedthrough so that (a) the MEMS chip is easily replaceable if it breaks, and (b) the MEMS chip can move beyond wiring cable limitations. Four features are underlined in the article: (1) MEMS itself can rectify the RF energy owing to the fact that the governing equation of the MEMS actuator involves the square of the voltage and/or current, thereby, ensuring higher system-level efficiency than any other RF transceiver circuits using additional rectifying components (e.g., diodes). (2) Both the transmitter and receiver use coils of the same design, whose sizes are equivalent to those of the MEMS actuators (hundreds of micrometers). Moreover, they can be operated at UHF, owing to the much higher self-resonant frequency ( $f_s > \text{GHz}$ ) when compared to conventional transmitters ( $f_s \approx \text{MHz}$ ). In addition, by using LCR resonant circuits, it is possible to not only (3) increase the transmission efficiency but also (4) multiply the driving voltage of the capacitive MEMS actuator, because of LC resonance. Voltage multiplication is quite useful for electrostatic MEMS operations because the movement is proportional to the square of the voltage across the MEMS capacitance. Comprehensive designs, implementations, and demonstrations of wireless operation are presented in this paper, for both thermal (resistive) and electrostatic (capacitive) actuators. Remote operation includes on-off-keying for MEMS without mechanical resonance and amplitude modulation of sinusoidal signals to stimulate the mechanical resonant frequency of MEMS.

© 2018 The Authors. Published by Elsevier B.V. This is an open access article under the CC BY license (<http://creativecommons.org/licenses/by/4.0/>).

### 1. Introduction – methods of wireless MEMS powering

Microactuators that interact with the surrounding environment have always been hot research topics since the 1980s. In 1990, Fujita proposed the concept of an arrayed microactuator that could interact with the environment cooperatively [1]. Microac-

\* Corresponding author at: Department of Electrical Engineering and Information Systems, Graduate School of Engineering, The University of Tokyo, 7-3-1, Hongo Bunkyo-ku, 113-8656 Tokyo, Japan.

E-mail address: [mems@if.t.u-tokyo.ac.jp](mailto:mems@if.t.u-tokyo.ac.jp) (Y. Mita).

URL: <http://www.if.t.u-tokyo.ac.jp> (Y. Mita).

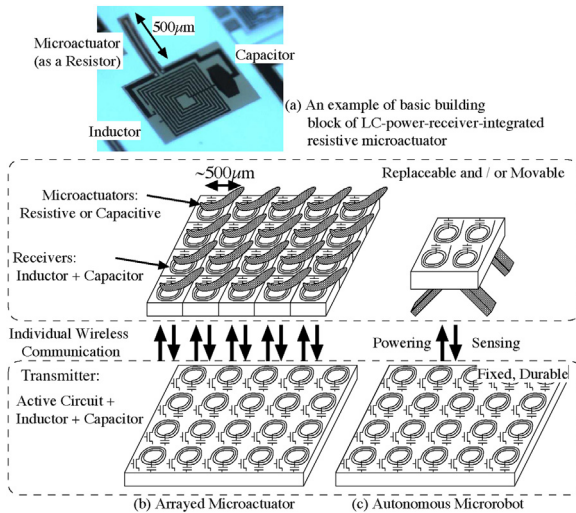


**Fig. 1.** Conceptual view of the proposed replaceable MEMS actuator.

tuators based on this concept were demonstrated by Ataka et al. in 1993 for use in cooperative microconveyance applications as ciliary motion microactuator arrays [2], which were arrays of thermal bimorph actuators. Then, several variants with different actuation principles were proposed. Konishi et al. in 1994 proposed a surface micromachined electrostatic air-flow actuator array [3], which was further improved using a deep-reactive ion etching (RIE) electrostatic valve [4], by Fukuta et al. in 2006. Another variant was the top-down inverted scratch drive electrostatic actuator [5] developed by Mita et al. in 1999. Micro (sub-centimeter-sized) self-movable machines have also attracted many MEMS researchers. Ebefors et al. demonstrated a walking inchworm MEMS robot in 1999 [6], which was based on a thermal bimorph actuator. Then, Hollar et al. demonstrated electrostatically driven long-range legs [7] for a walking robot in 2004, and Saito et al. demonstrated a sub-centimeter six-legs walking robot in 2013 [8]. Miki et al. demonstrated an alternating-magnetic-field-driven sub-centimeter MEMS helicopter in 1999 [9]. Uno et al., demonstrated in 2017 a wireless powering of ultrasonic-levitated 3.5 mm- $\phi$  hemispherical tiny object that they call “Luciola” [10]; an integrated LED was turned on and off by power conditioning LSI circuit. A couple of independent research groups presented pond-skating microrobots with electrowetting on dielectrics (EWOD). One of these was based on the swaying principle [11] by Chung et al., and the other was based on the bubble-jet principle by Mita et al. [12].

Fragileness and electrical energy feeding are the two common issues faced by microactuators that directly interact with the environment. Most of the above-mentioned actuators [2–8,11] were connected to power supplies through electrical wiring (also called as tethers). Wirings not only impeded the movement of autonomous robots but also inhibited the replacement of these MEMS actuators in case of breakage and/or malfunction. To solve these issues, in this article, the authors propose a micro wireless-powering scheme [13] as shown in Fig. 1. In the proposed scheme, each MEMS actuator is integrated with passive electrical components to form an LCR series resonant circuit (Fig. 1(a)). Another circuit with an LCR resonator is placed underneath, as a transmitter. The inductors of the transmitter and receiver are coupled through magnetic fields, and thus, power is transferred. The idea is to separate the system into a fragile (and/or moving) MEMS part and a fixed electrical powering (and/or sensing through powering) circuit part, and make the MEMS part replaceable (Fig. 1(b)) and/or self-movable (Fig. 1(c)). If the MEMS is broken, the engineer has to

physically replace the broken part only, without being bothered by the electrical wiring.

The third important feature of the proposed scheme is the size of the inductor and the operating frequency. The typical size of an LC tank circuit for both the transmitter and receiver proposed in this article is  $500\ \mu\text{m} \times 500\ \mu\text{m}$ , which is in the same order as that of the already-mentioned typical MEMS actuators. In fact, a smaller inductor can obtain a self-resonant frequency  $f_s$ <sup>1</sup> that can reach GHz values. In contrast, as summarized and compared in Table 1, most of previous MEMS researchers used relatively “big (centimeter-sized)” inductors in the transmitters and “medium (millimeter-sized)-to-big” ones in the receivers. These devices were driven by relatively low frequencies (in the 10 MHz range<sup>2</sup>) RF wave. In 2001, Takeuchi et al., demonstrated the teleoperation of two electrostatic microactuators [14,15] with a  $8.5\ \text{mm} \times 7.2\ \text{mm}$  20-turn planar receiver coil of  $4.8\ \mu\text{H}$  operated at 4.1 and 4.8 MHz. Mita’s EWOD microactuator [12] was driven with surface mount devices (SMDs) integrated on a  $5\ \text{mm} \times 8\ \text{mm}$  MEMS chip at 6.8 MHz. In 2015, Byun et al. demonstrated an EWOD driven by a planar printed circuit board (PCB) coil of 2.3 mm at 1.75 MHz [16]. Basset et al. developed a complete energy rectifier and control application-specific integrated circuit (ASIC) [17] and demonstrated 23 mW remote powering at 13.56 MHz with a  $20\ \text{mm} \times 20\ \text{mm}$  receiver coil of  $1.6\ \mu\text{H}$ . Sekitani et al. demonstrated 1.6–40 W power transfer using  $25\ \text{mm} \times 25\ \text{mm}$  planar transmitter and receiver coils at 13.56 MHz [18]. Takamiya developed a position-insensitive powering system by using a double-sized ( $50\ \text{mm} \times 50\ \text{mm}$ ) receiver on  $3 \times 3$  tiled matrices (yielding  $75\ \text{mm} \times 75\ \text{mm}$ ) of transmitter coils [19]. Laskovski and Yuce proposed a discrete transistor class-E oscillation circuit for wireless power to implants [21]. In the circuit, a  $100 \times 100\ \text{mm}$  8-turn planar inductor was integrated for the purpose of both oscillating feedback circuit and energy transfer. The circuit oscillated at 27 MHz, and RF power was transferred through 2 cm-thick lean beef to four-stacked  $15 \times 15\ \text{mm}$  7-turn coil having 30 MHz self resonant frequency [22], with 0.05% (–33 dB) of power efficiency. Another category is so-to-call “medium-sized coils” from Takahata’s group. Their coil size is sub-centimeter and working frequency is from 81.5 to 270 MHz. For example, Mohamed and Takahata integrated [23] shape-memory-alloy (SMA) microgripper with a  $4 \times 5\ \text{mm}$  9-turn coil made on polyimide film with resonant frequency of 140 MHz (with  $L = 184\ \text{nH}$  and  $C = 7\ \text{pF}$ ). By sending 0.2 W RF wave varying from 128 MHz to 150 MHz through 4 mm-diameter coil, temperature of the LC circuit increased due to residual resistance in the coil, and introduced phase change of the SMA.

Fig. 2 shows a thought comparison of RF powering to a “small” (MEMS-sized)  $500\ \mu\text{m}$ -diameter receiver (Rx) coil. Case (a) is an extension of the traditional method, in which the size of the transmitter (Tx) coil is in centimeters, and case (b) is the proposed method, in which the size of the Tx coil is the same as that of the Rx coil. Six steps of consideration (I)–(VI) can conclude that case (b) can produce a higher induction in the Rx coil.

- (I) **Tx self inductance  $L_1$** : In case (a), the Tx coil can be wound many times to obtain a higher Ampere-turn ( $nI$ ), whereas the number of turns is limited in case (b) owing to the planar nature and geometrical limitations. The typical values are  $100\ \mu\text{H}$  for (a) and  $10\ \text{nH}$  for (b).
- (II) **Total flux  $\Phi_1$  induced by  $L_1$** : A magnetic field  $B$  is generated by applying a current  $I$  to the Tx coil. The total flux is  $\Phi_1 = L_1 I$ , by

<sup>1</sup> The inductor is no more operational as  $L$  at frequencies above  $f_s$ , because of the parasitic parallel capacitance  $C_p$ .

<sup>2</sup> Frequency of 3–30 MHz, named “HF” (high frequency) band by the International Telecommunication Union Recommendation (ITU-R V.431-7).

**Table 1**

Comparison of conventional and proposed power transfer schemes.  $D$ : diameter,  $n$ : coil turns,  $L$ : inductance,  $f_s$ : self-resonant frequency. Shape labels are defined as: sq.: square, sol.: solenoidal, oct.: octagonal, SMD: surface mount device, ro.: round, rect.: rectangular, n.a.: the value is neither available in the article, nor extractable. \*: extracted by the author from the values shown in articles.

ID	Transmitter				Receiver					
	Shape	$D$ [mm]	$n$	$L$ [H]	Shape	$D$ [mm]	$n$	$L$ [H]	$f_s$ [Hz]	Working freq. [Hz]
Takeuchi01 [15]	sq.	80	14	25 $\mu$	sq.	8	20	4.8 $\mu^*$	15 M	4.1–6.9 M
Basset07 [17]	sol.	70	4	n.a.	sq.	15	16	5.8 $\mu^*$	27 M	13.56 M
Sekitani07 [18]	oct.	25	13	3 $\mu$	oct.	25	38	20 $\mu$	n.a.	13.56
Mita07 [12]	sol.	50	10	3.65 $\mu^*$	SMD	–	–	3.3 $\mu^*$	n.a.	6.8 M
Laskovski11 [21]	sq.	100	8	2.7 $\mu$	–	–	–	–	–	–
[22]	–	–	–	–	4 $\times$ sq.	15	7	n.a.	30 M	27 M
Ali10 [23]	sol.	4	n.a.	497 n	sq.	5	9	184 n	n.a.	128–140 M
Ali13 [25]	sol.	4	n.a.	497 n	sq.	6*	4	45 n	1 G*	200–270 M
Fuketa14 [20]	oct.	40	7	n.a.	oct.	40	7	n.a.	n.a.	13.56 M
Chee15 [27]	n.a.	6	n.a.	213 n	rect.	7 $\times$ 5	n.a.	570 n	n.a.	81.5 M
Byun15 [16]	sol.	23	5	5.8 $\mu$	sq.	2.3	50	42 $\mu$	n.a.	1.75 M
Uno18 [10]	sol.	31	5	1.25 $\mu$	ro.	3	2.5	22.7 n	n.a.	12.3 M
Proposed [13]	sq.	0.52	5.5	12 n	sq.	0.52	5.5	12 n	6.1 G	750 M, 1 G

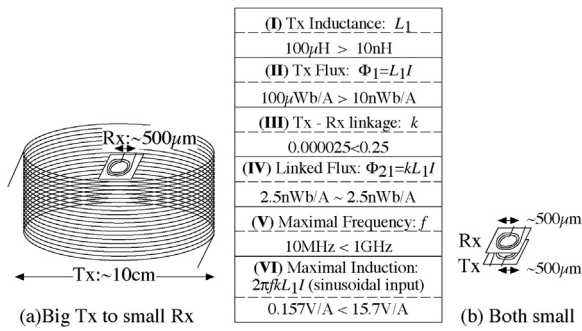


**Fig. 2.** Performance comparison of sending RF power (a: conventional) from big transmitter (Tx) coil to small receiver (Rx) coil and (b: proposed) from small Tx coil to small Rx coil.

definition, yielding 100  $\mu\text{Wb/A}$  for (a) and 10 nWb/A for (b). In the following discussion, the amount of current  $I$  is kept arbitrary, therefore, all units are represented as per unit Ampere [A].

(III) **Amount of flux linked to the Rx coil  $\Phi_{21}$ :** However, not all the flux induced by  $L_1$  can be linked to the Rx coil. The linked flux is precisely given by the integral of the magnetic field  $B$  and the area element  $dA$ ; in the case of air-core coils, the coupling coefficient  $k$  can be assumed to be roughly proportional to the area ratio.<sup>3</sup> It means that even though the “big” Tx coil excites larger total flux, only a small portion actually links with the Rx coil. In the case of (a), the coupling coefficient can be as low as 0.000025 ( $\therefore 0.25^2 \pi / 50^2 \pi$ ), whereas, in the case of (b), the value can be much larger, for example, up to 0.25. The magnetic field linking to the Rx coil is therefore 2.5 nWb/A for both cases.

(IV) **Maximal frequency and voltage by induction V:** The energy is transferred by electromagnetic induction, and the amount transferred is proportional to the time derivative of the linked field:  $V = d\Phi/dt$ . By assuming sinusoidal current in Tx ( $I = I_0 \sin 2\pi ft$ ), the amount is proportional to  $2\pi f \Phi_{21}$ . Therefore, the guiding principle is that a higher frequency is better for transfer; however, it cannot exceed the self-resonant frequencies  $f_s$  of the Tx and Rx coils. Moreover, the more Ampere-turns the coil has (to increase  $\Phi_{21}$ ), the higher the self inductance  $L_1$  and parasitic capacitance  $C_{p1}$  between the wirings will be, and thus, the self-resonant frequency will

<sup>3</sup> When assuming a finite-length solenoid, the magnetic field  $B$  is stronger at the coil center, and therefore, the coefficient can be bigger. However the value stays in the same order of magnitude.

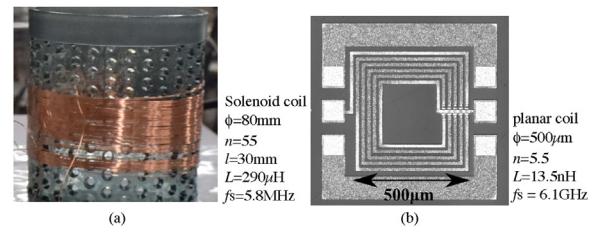


**Fig. 3.** Typical “Big” and “Small” coils made by the authors. (a) An 8 cm- $\phi$ , 3 cm-long, 55-turn solenoid coil with 0.4 mm  $\phi$  polyurethane copper wire (UEW) with  $L=290\mu\text{H}$  and  $f_s=5.8\text{MHz}$ . (b) A 500  $\mu\text{m}$ - $\phi$ , 5.5-turn planar coil made on fused silica substrate, with  $L=13.5\text{nH}$  and  $f_s=6.1\text{GHz}$ .

be lower ( $\therefore f_{s1} = 1/2\pi\sqrt{L_1 C_{p1}}$ ). A measurement example is shown in Fig. 3(a): A centimeter-sized solenoid coil has approximately 10 MHz of  $f_s$ . On the contrary, a small-sized coil has over several GHz of  $f_s$ , as demonstrated in case (b), which has 6.1 GHz of  $f_s$ . Therefore, (a) the “big” coils can be operated nominally at approximately 10 MHz and (b) the “small” coils can be operated up to 1 GHz, yielding (a)  $V=0.157\text{V/A}$  and (b)  $15.7\text{V/A}$ , respectively.

The above consideration is further extended in Section 2 to provide a general guideline of the integrated coil design. Following the guideline top-down, a MEMS designer can derive the geometry of the coil (i.e., loop number and line width) for the required performance such as the energy transfer efficiency, under the process restrictions. The details of the fabrication of coils and capacitors and the remote power transfer experiment are reported in Section 3.

Another important feature of this article is that our scheme does *not* require *any additional electrical components* to rectify the energy. Many existing reports use a diode and decoupling capacitor to generate direct current (DC) voltage initially, and then, some switching circuitry is added for MEMS control [17], as shown in Fig. 4. We underline that *because MEMS, by nature, works with the square of the electrical input, i.e., current or voltage, it can act as a rectifying component*. This means that, we do not have to generate a DC voltage; we only have to apply an alternating current (AC) to drive the MEMS, because the MEMS actuator generates a mechanical force, *regardless of its direction* (positive or negative). In practice, we only have to introduce MEMS as one of the LCR series resonant circuit components. In the case of resistive (thermal type) actuators, the actuator is the R component, and L and C are integrated with it, as shown in Fig. 4(b). Such a configuration always provides the maximum efficiency because of the absence of

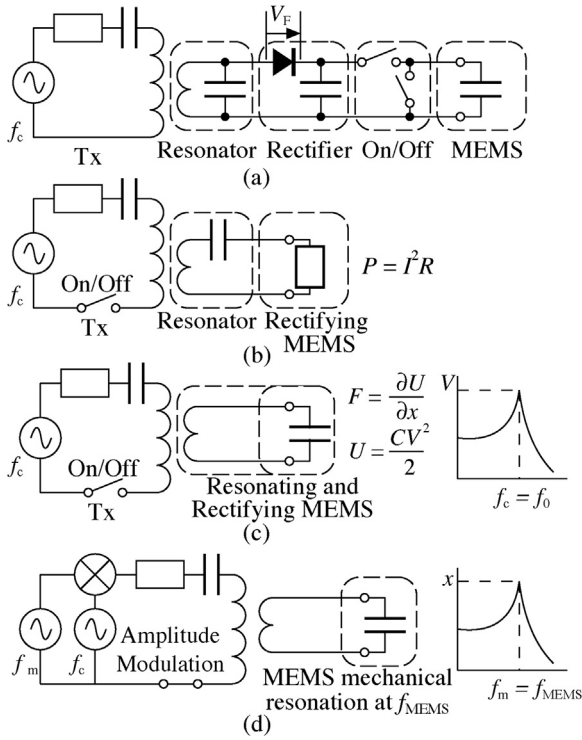


**Fig. 4.** (a) Conventional wireless energy transfer scheme. (b) Proposed scheme that uses MEMS itself as an energy rectifier, as a resistance in the LCR series resonance circuit. (c) Another implementation that uses capacitive MEMS as a part of the resonance circuit. (d) Amplitude modulation (AM) operation of MEMS that can obtain a larger displacement at the mechanical resonant frequency  $f_{MEMS}$ .

additional components such as diodes whose forward voltage ( $V_F$ ) produces certain power losses. To date, several reports of thermal actuator remote powering are found in literature. In 2009, Li et al. presented a Parylene-based Electrothermal Valve integrated with 10 mm- $\phi$  wound inductor with matching capacitor, for remote drug delivery experiment with a mouse [24]. Following the SMA gripper demonstration [23], Takahata's group realized a couple of thermal microactuators: Ali et al. proposed in 2013 a SMA spiral coil actuator of approximately 6  $\times$  6 mm. The coil moved out-of-plane direction and formed a 466  $\mu$ m-high pyramidal shape at 233 MHz RF wave [25]. In 2015, Fong et al. presented a 9.2  $\times$  2.7 mm-sized spiral SMA bimorph actuator driven at 185 MHz [26], and Ali et al. presented a thermo-pneumatic micropump heated by 7  $\times$  5 mm-sized spiral inductor of 570 nH and 6.69 pF of integrated capacitor at 81.5 MHz [27]. In the same year, we demonstrated a 500  $\times$  20  $\mu$ m-sized polyimide bimorph (ciliary motion) microactuator by 520  $\times$  520  $\mu$ m spiral inductor at 1 GHz [13]. The on-off-keying (OOK) demonstration of a ciliary motion actuator providing 15.8% power efficiency is presented in Section 4.

Section 5 demonstrates MEMS remote operation in the case of capacitive (electrostatic type) actuators. Capacitive MEMS can be a C part of the LCR resonant receiver circuit, as shown in Fig. 4(c). It is because the typical value of the MEMS microactuator device is approximately 1 pF, and with a typical MEMS-sized inductance (10 nH), the resonant frequency yields 1.59 GHz. A bonus for MEMS operation as the capacitive load of a series resonance circuit is the voltage multiplication by the LCR circuit at the resonance frequency. Moreover, a capacitive MEMS such as a comb-drive actuator with silicon springs often has mechanical resonance behavior. At the resonant frequency  $f_{MEMS}$ , a movement larger than its intrinsic movement (defined by  $x = F/k$ ) is obtainable. Such an operation is possible by amplitude modulating (AM) the carrier wave at the MEMS operation frequency, as shown in Fig. 4(d). Note that a nom-

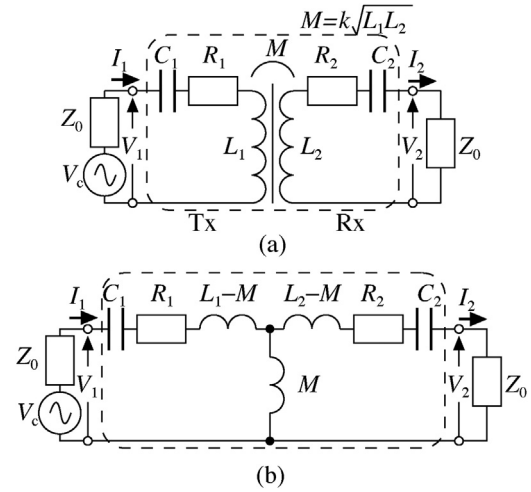


**Fig. 5.** (a) Equivalent circuit of wireless energy transfer system. (b) Its T-equivalent expression.

inal MEMS operating signal frequency  $f_m$  is in the order of several kHz so that the carrier frequency  $f_c$ , which is the circuit resonant frequency, can be chosen independently.

## 2. Design of energy transfer inductor for MEMS integration

In this section, a top-down design methodology is discussed. The design mainly refers to inductor design. We use Imura's approach [28] to express the system using a T-shape equivalent circuit, as shown in Fig. 5. The model in the Kurs et al.'s paper [29] was not used because their decay-based model was useful for physical understanding but was not practical for electrical circuit analysis. The maximum power transfer efficiency  $\eta_{21} = |S_{21}|^2$  and its relationship with the coupling coefficient  $k$  is discussed at first.  $S_{21} = 2V_2/V_c$  is the forward voltage gain in the scattering matrix [30]. Then, two cases in which a part of the components in the secondary (receiver) circuit is replaced by either resistive or capacitive MEMS are analyzed. Based on such circuit-level understanding, a MEMS-sized inductor design methodology is discussed. The role of the MEMS designer is to find the best combination for the tradeoff between the characteristic values, under the system requirements and restrictions of the fabrication process and driving circuitry.

### 2.1. Transfer power analysis

In the equivalent circuit (Fig. 5),  $L_1$  and  $L_2$  are inductors with series parasitic resistances of  $R_1$  and  $R_2$ , respectively. They have a mutual inductance  $M$  due to the linked field:  $M = k\sqrt{L_1L_2}$ .  $C_1$  and  $C_2$  are external capacitances for series resonance. The source and load resistances are both denoted as  $Z_0$ , and in the case of resistive MEMS, the microactuator takes a part of  $Z_0$  at the Rx side. According to the premise in this article, identical coils are used for both transmitter and receiver ( $\therefore L_1 = L_2 = L$ ,  $R_1 = R_2 = R$ ) and in order to match the frequency of both the Tx and Rx, capacitances must be the same, i.e.,  $C_1 = C_2 = C$ .  $S_{21}$  is calculated to be:

$$S_{21} = \frac{2V_2}{V_c} = \frac{2j\omega MZ_0}{\omega^2 M^2 + [(R + Z_0) + j(\omega L - \frac{1}{\omega C})]^2}, \quad (1)$$

where  $j^2 = -1$ . At the intrinsic resonant frequency  $\omega_0 = 1/\sqrt{LC}$ ,

$$S_{21} = \frac{2j\omega_0 MZ_0}{\omega_0^2 M^2 + (R + Z_0)^2} = \frac{2jZ_0}{\omega_0 M + (R + Z_0)^2/\omega_0 M} \quad (2)$$

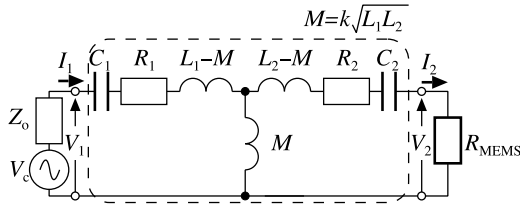


Fig. 6. T-equivalent circuit of wireless energy transfer system to drive thermal MEMS actuator.

By considering Eq. (2) as a function of  $\omega_0 M (>0)$ , the maximum value

$$S_{21} = \frac{jZ_0}{Z_0 + R} \quad (3)$$

or

$$|S_{21}| = \left| \frac{1}{1 + R/Z_0} \right| \quad (4)$$

is obtained at

$$\omega_0 M = \frac{(R + Z_0)^2}{\omega_0 M} \quad (5)$$

$$\therefore k = \frac{M}{L} = \frac{R + Z_0}{\omega_0 L} \quad (6)$$

It should be noted that by analyzing the impedance  $Z_{11} = V_1/I_1$  at the limit of  $Z_0, R \rightarrow 0$ , two split resonant frequencies can be observed. The phenomenon is not directly used in the applications of this article.

$$\omega_{L,H} = \frac{1}{\sqrt{(L \pm M)C}} \quad (7)$$

### 2.2. Wireless energy transfer circuit applied to resistive MEMS

To apply the circuit to a resistive load, we replace the output load  $Z_0$  with  $R_{MEMS}$ , as shown in Fig. 6. The power dissipation in  $R_{MEMS}$  is given by  $P_{MEMS} = R I_2^2$ , where  $*$  denotes a complex conjugate number. Therefore, the maximum output current  $I_2$  gives the maximum actuation of the resistive MEMS.  $I_2$  is given by the following equation:

$$I_2 = \frac{j\omega M}{(\omega M)^2 + [(Z_0 + R_1) + j(\omega L_1 - \frac{1}{\omega C_1})]} \left[ (R_{MEMS} + R_2) + j(\omega L_2 - \frac{1}{\omega C_2}) \right] V_1 \quad (8)$$

Presuming identically sized coils, the maximum value is obtained at  $\omega_0 = 1/\sqrt{LC} = 1/\sqrt{L_1 C_1} = 1/\sqrt{L_2 C_2}$  as:

$$I_2 = \frac{j\omega_0 M}{(\omega_0 M)^2 + (Z_0 + R_1)(R_{MEMS} + R_2)} V_1 \quad (9)$$

$$= \frac{j}{\omega_0 M + \frac{(Z_0 + R_1)(R_{MEMS} + R_2)}{\omega_0 M}} V_1 \quad (10)$$

Considering the fact that  $\omega_0 M > 0$ , Eq. (10) takes the maximum value at the following condition:

$$\omega_0 M = \frac{(Z_0 + R_1)(R_{MEMS} + R_2)}{\omega_0 M}, \quad (11)$$

which gives the relationship between the resonant frequency, inductance, coupling coefficient, and resistances:

$$k\omega_0 \sqrt{L_1 L_2} = \sqrt{(Z_0 + R_1)(R_{MEMS} + R_2)}. \quad (12)$$

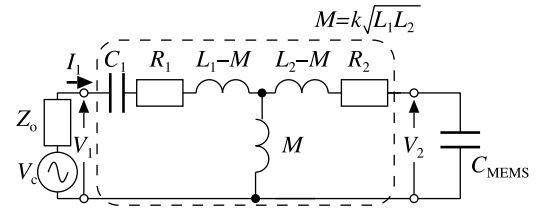


Fig. 7. T-equivalent circuit of wireless driving system for capacitive MEMS actuator.

The maximum power consumed in the microactuator is therefore derived to be:

$$P_{MEMS} = R_{MEMS} I_2^2 = \frac{R_{MEMS}}{4(Z_0 + R_1)(R_{MEMS} + R_2)} V_1^2. \quad (13)$$

Eq. (13) demonstrates that no rectifier device such as diode is necessary for driving a resistive MEMS. Interestingly, the maximum power can be defined by the output impedance of the transmitter, regardless of the resistance of MEMS itself, by minimizing the parasitic resistances  $R_1$  and  $R_2$ .

### 2.3. Capacitive MEMS driving system analysis

Fig. 7 shows a T-equivalent circuit for capacitive MEMS driving. The idea is to use the MEMS capacitance as a part of the receiver LCR circuit. The capacitance required for MEMS actuation can be derived top-down using the virtual displacement method: The actuator force is given by a derivative of the stored energy  $U = CV^2/2$  by the variable of examining orientation. The typical value is in the sub-pF range. The anchor electrode often has a bigger parasitic capacitance; a  $150 \mu\text{m} \times 150 \mu\text{m}$  anchor electrode over a  $1 \mu\text{m}$   $\text{SiO}_2$  insulator<sup>4</sup> gives a parasitic capacitance of 0.74 pF to the substrate. The working MEMS (variable) and parasitic anchor (fixed) capacitances constitute the total MEMS capacitance  $C_{MEMS}$ .

The voltage across  $C_{MEMS}$  is given by the following equation:

$$V_2 = \frac{M}{C_{MEMS}} \frac{1}{(\omega M)^2 + [(Z_0 + R_1) + j(\omega L_1 - \frac{1}{\omega C_1})]} \frac{V_1}{\left[ R_2 + j(\omega L_2 - \frac{1}{\omega C_{MEMS}}) \right]} \quad (14)$$

The imaginary part in Eq. (14) can be canceled at the resonant frequency  $\omega_1 = 1/\sqrt{L_1 C_1} = 1/\sqrt{L_2 C_{MEMS}}$ . The voltage across the MEMS yields:

$$V_2 = \frac{M}{C_{MEMS}} \frac{1}{(\omega_1 M)^2 + (Z_0 + R_1)R_2} V_1 \quad (15)$$

By rearranging the equation with  $L = L_1 = L_2, C = C_{MEMS} = C_1$ , and  $\omega_1 = 1/\sqrt{LC}$  and  $M = kL$ ,

$$V_2 = \frac{1}{k + \frac{(Z_0 + R_1)R_2 C_{MEMS}}{kL}} V_1 \quad (16)$$

Eq. (16) gives its maximum value:

$$V_2 = \frac{1}{2k} V_1 = \frac{1}{2\sqrt{\frac{(Z_0 + R_1)R_2 C_{MEMS}}{L}}} \quad (17)$$

at the following condition

$$k = \frac{(Z_0 + R_1)R_2 C_{MEMS}}{kL}. \quad (18)$$

<sup>4</sup> Relative permittivity is assumed to be 3.7.

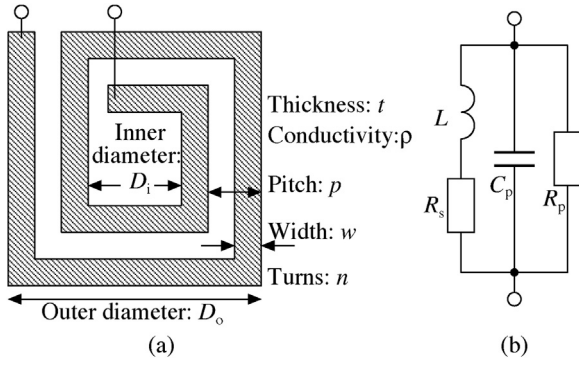


**Fig. 8.** (a) Geometries of the planar coil for algebraical inductance and resistance estimations. (b) Equivalent circuit used in this article.

Eq. (17) demonstrates the possibility of not only capacitive remote powering but also voltage multiplication. For example, for a coupling coefficient  $k=0.05$ , it is possible to obtain 10 times voltage multiplication of the applied voltage  $V_2$  across the MEMS capacitor.

#### 2.4. Resistance and inductance of planar coil

Eqs. (4), (13), and (17) show that more power is transferred if the series parasitic resistance  $R$  is small. However, there is a tradeoff between the series resistance and the self inductance: A higher turn number  $n$  may produce higher  $L$ , but the wire becomes longer and narrower under a fixed size, resulting in a larger  $R$ . The designer must therefore find the best combination for such a tradeoff. We assume a square planar coil in this article, as shown in Fig. 8(a). The equivalent circuit can be expressed as shown in Fig. 8(b). Among the equivalent circuit components, the inductance  $L$  and series resistance  $R_s$  are the most important ones because  $L$  dominates the frequency for energy transfer and  $R_s$  dominates the transfer loss of energy transfer. These two values can be calculated algebraically from geometrical values.

According to Neagu et al., the inductance of a planar square coil is given by the following equation [33]:

$$L = \frac{\mu_0 D_o^3}{4\pi p^2} (1 - \alpha^2)(1 - \alpha) \left[ \ln \frac{1 + \alpha}{1 - \alpha} + 0.2235 \frac{1 - \alpha}{1 + \alpha} + 0.726 \right], \quad (19)$$

where  $\mu_0$ ,  $D_o$ ,  $p$ , and  $\alpha$  are the magnetic permeability ( $4\pi \times 10^{-7}$  H/m), outer diameter, pitch of the wiring, and ratio of inner and outer diameters  $D_i/D_o$ , respectively. The inner diameter  $D_i$  is given by the following equation:

$$D_i = D_o - 2w - 2p(n - 1). \quad (20)$$

The series resistance  $R_s$  is given by the total length  $l$ , width  $w$ , thickness  $t$ , and resistivity  $\rho$  of the wiring material. The total length of the winding is given by:

$$l = \left\{ \sum_{i=1}^n 4[D_o - 2(i - 1) - w] \right\} - p = 4n(D_o - w + p - pn) - p. \quad (21)$$

Therefore, the total resistance is given by the following equation:

$$R = \frac{\rho}{wt} [4n(D_o - w + p - pn) - p], \quad (22)$$

Another important part of the coil is the parasitic capacitance  $C_p$  that gives the parallel self resonance of the inductor; however, the value depends highly on the environment, including substrate material, thickness, etc. Therefore, in this article, the value was roughly estimated first by simulation using 3D CAD (Keysight ADS), and then, the precise value was extracted by fitting the measured data. The parallel resistor  $R_p$ , which dominated the equivalent

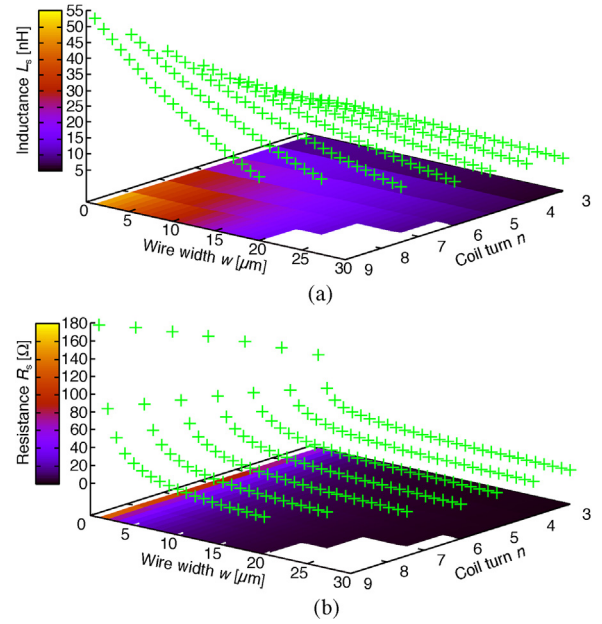


**Fig. 9.** (a) Inductance  $L$  and (b) resistance  $R$  as functions of coil turn  $n$  and width  $w$ .

inductance near the parallel resonance frequency, was not taken into account in the CAD simulations and was extracted only by post-fitting.

#### 2.5. Examination of possible combinations of inductance and resistance

Before searching for an optimal condition, it is worthwhile to observe the tradeoff between the obtainable inductance and resistance. The number of coil turns  $n$  and wiring width  $w$  are the two variables that MEMS designers can define by themselves. The other values are technology-dependent process parameters. The process parameters used in this article were defined by presuming an integrated circuit (IC) process as follows: (1) Thickness:  $t=2.4 \mu\text{m}$ , which was realized by a two-level metal process, (2) Material: Aluminum,  $\rho=27.8 \text{ n}\Omega\text{m}$  at 300 K. (3) Gap between electrodes:  $10 \mu\text{m}$ , yielding  $p = w + 10$ , which was defined mainly by the lithography process limitations. Among the design parameters,  $D_o$  was defined to be  $520 \mu\text{m}$ , so that the size of the coil was equivalent to that of typical MEMS, for example, the ciliary motion actuator presented in Section 4. The substrate was chosen to be fused silica,  $500 \mu\text{m}$  in thickness; however, it does not directly appear in the analyses in this paper.

Fig. 9(a) and (b) shows the calculated relationships of inductance and resistance, respectively. The points were calculated using a spreadsheet program (GNU gnumeric version 1.12.11) and plotted using a graphing utility (GNUplot version 4.6 patchlevel 5). In the calculations, the coil turn  $n$  was varied from  $n=3$  to  $n=9$ , and the width  $w$  was increased from  $w=1 \mu\text{m}$  to  $30 \mu\text{m}$  in steps of  $1 \mu\text{m}$ . The values varied from  $(L, R_s) = (5.21 \text{ nH}, 1.88 \Omega)$  at  $(n, w) = (3, 30 \mu\text{m})$  to  $(L, R_s) = (53.0 \text{ nH}, 180 \Omega)$  at  $(n, w) = (9, 1 \mu\text{m})$ . The trend could be observed more clearly by plotting  $R_s$  as a function of  $L$ , as shown in Fig. 10. The solid lines on the figure were directly calculated by the GNUplot graphing utility using equations, thereby confirming the calculations and showing the dependency on coil turns more clearly. The general trend was that the parasitic resistance  $R_s$  increased inversely proportional to the coil width, and proportional to the the turn number.  $L$  and  $R_s$  followed the same trend: the higher the  $L$ , the higher the  $R_s$ . The curvature of the plot indicated the existence of some optimal values.

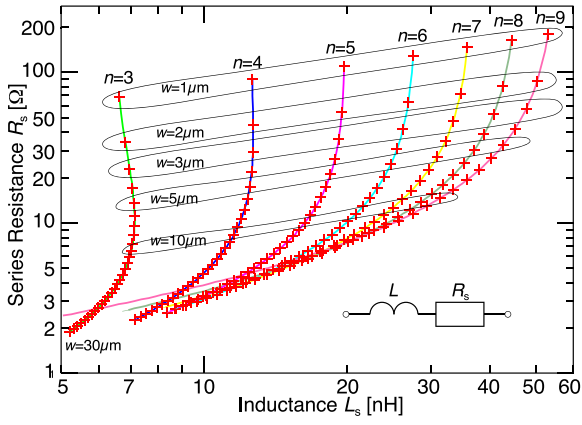


Fig. 10. Relationship of inductance  $L$  and resistance  $R$ .

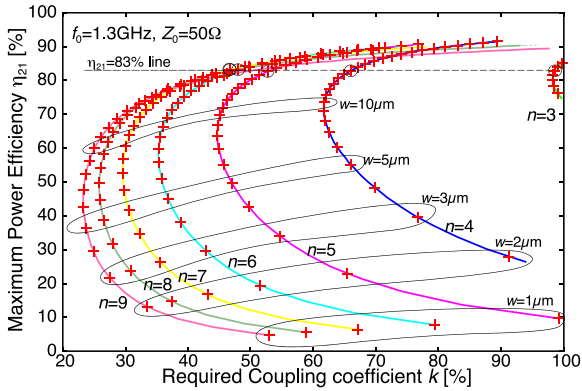


Fig. 11. Coupling coefficient  $k$  and obtainable maximum efficiency  $\eta_{21}$  for  $Z_0 = 50 \Omega$ ,  $f_0 = 1.3 \text{ GHz}$ .

2.6. Finding optimal value for given restrictions

By constraining the combinations of  $L$  and  $R_s$ , the maximum power efficiency  $\eta_{21} = |S_{21}|^2$  and the required coupling coefficient  $k$  could be calculated, as shown in Fig. 11. The source and load resistances  $Z_0 = 50 \Omega$  and the energy transfer frequency  $f_0 = \omega_0/2\pi = 1.3 \text{ GHz}$  were given as the system boundary conditions.<sup>5</sup>  $S_{21}$  and  $k$  were calculated using Eqs. (4) and (6), respectively. The graph clearly shows the existence of  $k$  values for which the power transfer efficiency can exceed 80% when using the chosen MEMS-sized microinductors ( $D_0 = 520 \mu\text{m}$ ).

The MEMS designer can choose an appropriate combination of coupling coefficient and maximum power efficiency according to the system requirement, and then, the geometry of the coil can be selected top-down. For example, there are six possible combinations to satisfy  $\eta_{21} = 83\%$ , as shown in Fig. 11. By summarizing the candidates in Table 2, a certain amount of saturation is observed between five and six turns. It is, therefore, reasonable to choose values in this area.

3. LC transceiver fabrication and power transfer efficiency measurement

Inductors were fabricated through a standard lithography process on a 500- $\mu\text{m}$ -thick fused silica substrate. The process used a 1.2- $\mu\text{m}$ -thick two-layer aluminum metal and 1- $\mu\text{m}$ -thick sput-

Table 2  
Possible inductor designs to satisfy  $\eta_{21} = 83\%$ .

Coil turns	3	4	5	6	7	8
Width $w$ [ $\mu\text{m}$ ]	13	16	18	20	21	21
$L$ [nH]	6.82	10.2	12.8	14.0	14.4	14.4
$R_s$ [ $\Omega$ ]	4.91	4.92	5.00	4.84	4.81	4.96
$\eta_{21}$ [%]	82.9	82.9	82.6	83.1	83.2	82.7
$k$ [%]	98.6	66.0	48.0	46.7	46.7	46.6
$C$ [pF]	2.198	1.47	1.17	1.07	1.04	1.04

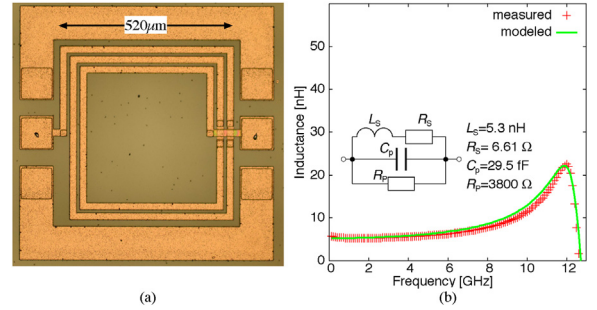


Fig. 12. (a) Photomicrograph of 2.5-turn coil and (b) frequency dependence of inductance.

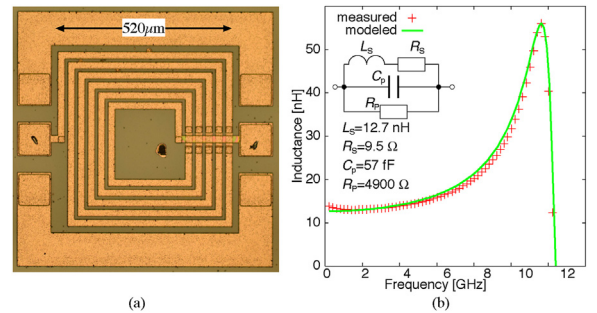


Fig. 13. (a) Photomicrograph of 5.5-turn coil and (b) frequency dependence of inductance.

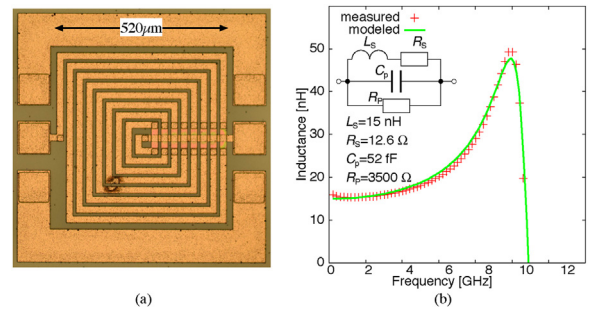


Fig. 14. (a) Photomicrograph of 8.5-turn coil and (b) frequency dependence of inductance.

tered  $\text{SiO}_2$  insulator. Figs. 12(a), 13(a), and 14(a) show the fabricated coils with 2.5, 5.5, and 8.5 turns. The designed values are as follows: outer diameter  $D_0 = 520 \mu\text{m}$ , wire width  $w = 20 \mu\text{m}$ , and pitch  $p = 30 \mu\text{m}$ . The chip was designed to be measured using a vector network analyzer (VNA, Keysight Technologies N5247A). A ground-signal-ground (GSG) probe (Cascade Microtech, ACP50) was used to contact the pads. In order to measure inductors through a pair of GSG probes, the two ports of the inductor (i.e. current inlet and outlet) had to be placed at the opposite side. Such design is not only widely deployed for RF inductors [31,32] but also practically very useful to create a series resonant circuit; Consequently, the

<sup>5</sup> In this project, an amateur radio transceiver in the 1296 MHz band was initially planned to be used as the power source.

**Table 3**

Measured and calculated inductance. Meas: Measured, Eq. (1): Neagu's model [33], Eq. (2): Adapted Wheeler's model [35], Eq. (3): Current sheet approximation, Eq. (4): Data fitted monomial expression. Eqs. (2)–(4) were from [34].

$n$	Meas [nH]	Eq. (1) [nH]	Eq. (2) [nH]	Eq. (3) [nH]	Eq. (4) [nH]
2.5	5.3	4.6	6.00	6.13	6.16
		(−15%)	(+12%)	(+14%)	(+14%)
5.5	12.7	13.1	15.0	14.83	14.76
		(+3%)	(+15%)	(+14%)	(+14%)
8.5	15.0	15.3	16.9	17.54	16.24
		(+2%)	(+11%)	(+14%)	(+8%)

spiral coil turn numbers in the following experiments were not an integral number but integral and half.

### 3.1. Equivalent circuit extraction

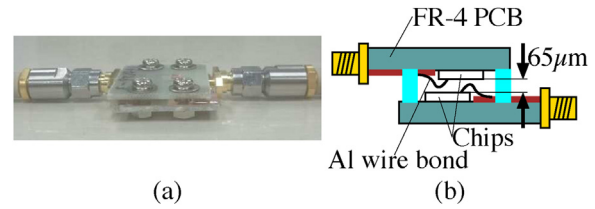
Calibration was done using the short, open, load ( $50\Omega$ ), and through structures in an impedance standard substrate (Cascade Microtech, 101-190). On the same chip, there were three identical devices for each design, and the S-matrix measurement results of each design were averaged. The S parameters were then converted to admittance matrices  $Y$  and the impedances of the coils were calculated by  $Z_{DUT} = -1/Y_{12} = \alpha + j\beta$ . Then, the inductances were calculated by assuming that the imaginary part came from the inductance ( $j\beta = j\omega L \rightarrow L = \beta/\omega$ ) as plotted in Figs. 12(b), 13(b), and 14(b). In each figure, the  $L$  portion calculated based on the model is plotted with a green line. The fitting results show that a simple series resistance  $R_s$ , parallel parasitic capacitance  $C_p$ , and limiting parallel resistance  $R_p$  model can well express the frequency response of the coil.

Table 3 compares the extracted inductances with algebraical calculations. In addition to the inductance value with Neagu et al.'s model [33] that we used in the previous sections for energy transfer efficiency estimation, those with three models derived by Mohan et al. [34] were calculated. The additional models were adapted Wheeler's model [35] (denoted as Eq. (2) hereafter), current sheet approximation (Eq. (3)), and data fitted monomial expression (Eq. (4)). In Mohan's paper, non-integer coil turns (such as 6.5 and 5.75) were used. Therefore we considered that the equation was applicable to our case (i.e. half integer) as well. The discrepancy in between the extracted and calculated inductances varied from −15 to +15% for all the cases. Mohan disclosed their “measured” 61 inductors table<sup>6</sup> in his article [34], and we could statistically benchmark the absolute error of his models. The values were −4 to +6%, −4 to +10%, and −30 to +18% for Eq. (2), Eq. (3) and Eq. (4), respectively. Also by taking the fact that Mohan's “measured” values were in fact calculated results of field solver, it can be said that our strategy of taking Neagu's equation could give values within a reasonable error.

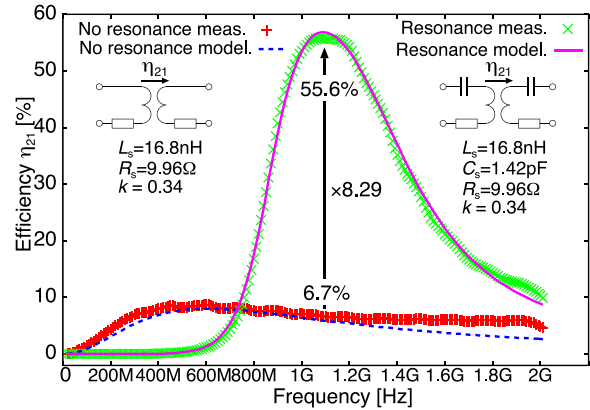
### 3.2. Wireless power transfer experiment

Fig. 15(a) shows a photograph of the wireless energy transfer measurement. The forward voltage gain  $S_{21}$  was measured using a pair of 5.5-turn coil chips. The chip was mounted on an FR-4 type (glass epoxy) PCB, and was wire-bonded with  $25\mu\phi$  aluminum wire using a manual wedge bonder (WestBond 7476D). The chips were aligned face-to-face and fixed with a screw of  $3\text{mm}\phi$  to stabilize the measurement. The gap between the coil surfaces was  $65\mu\text{m}$ , as illustrated in Fig. 15(b).

As shown in Fig. 16, the energy efficiency  $\eta_{21} = |S_{21}|^2$  was calculated from the measurement. Two cases were tested: (a) Simple induction i.e., without series capacitance, which produced a



**Fig. 15.** Two 5.5-turn  $D_o = 520\mu\text{m}$  coil antennas were coupled face-to-face and the wireless forward voltage gain was measured by a VNA. (a) Photograph and (b) schematic view.



**Fig. 16.** Wireless energy transfer efficiency of resonant mode (with capacitance, solid line) and non-resonant mode (without capacitance, broken line).

maximum efficiency of 6.7%. (b) By adding a 1 pF on-chip metal (Al)–insulator ( $\text{SiO}_2$ )–metal (Al) series capacitor next to the inductor (on the same substrate) at each side, the efficiency was increased 8.3 times (to 55.6%). It is because the inductive term in the efficiency equation was canceled by the series capacitance. From 1.03 GHz to 1.18 GHz, the resonant efficiency had a plateau with the highest value. The bandwidth measured from the −3 dB points ( $P = 0.5P_{\text{max}}$ ) was 669 MHz (846 MHz to 1.515 GHz). The simplest model, shown in Fig. 5 and calculated using equation (1), showed a good approximation. The obtained parameter values were slightly higher than the intrinsic ones:  $L$  by 4.1 nH (12.7–16.8 nH),  $C$  by 0.42 pF (1–1.42 pF), and the series parasitic resistance  $R_s$  by  $0.46\Omega$  ( $9.5\Omega$  to  $9.96\Omega$ ).<sup>7</sup> By another measurement, the wire bonding of approximately 2 mm length, to connect the device to the FR-4 PCB line, was measured to be  $L = 2.1\text{ nH}$  and  $R = 0.18\Omega$ . Therefore, the main cause of the  $L$  and  $R$  increases could be attributed to the bonding wires ( $: 2.1 \times 2 = +4.2\text{ nH}$ ,  $0.18 \times 2 = +0.36\Omega$ ). The real cause of the increase in  $C$  is kept, and to explain in detail is out of the scope of this article. Instead,  $C$  was fitted post-measurement, together with the coupling coefficient  $k$ . In summary, we could conclude that, highly efficient (55.6%) RF energy transfer was performed for  $Z_0 = 50\Omega$  with a moderate coupling coefficient  $k = 0.34$ .

## 4. Resistive microactuator on–off remote operation

The coupled LC circuit used in the previous section was connected in series to a thermal actuator off the chip. The LC circuit and actuators were fabricated separately on different chips and were connected by wire bonding. As shown in Fig. 17, the actuator was made on a standard Si wafer with two different types of polyimide layers with low and high coefficients of temperature expansions, which sandwiched a Cr/Au resistance (heater) line

<sup>7</sup> Limiting parallel resistor  $R_p$ , identified in Fig. 13 was not considered because it was not dominant in the used frequency range.

<sup>6</sup> Table IV of the article [34].

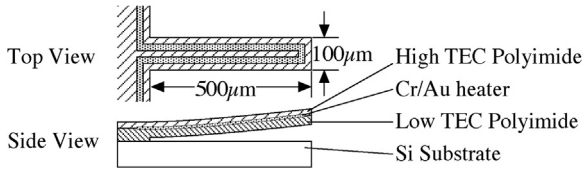


Fig. 17. Schematic view of a resistive (ciliary motion) microactuator.

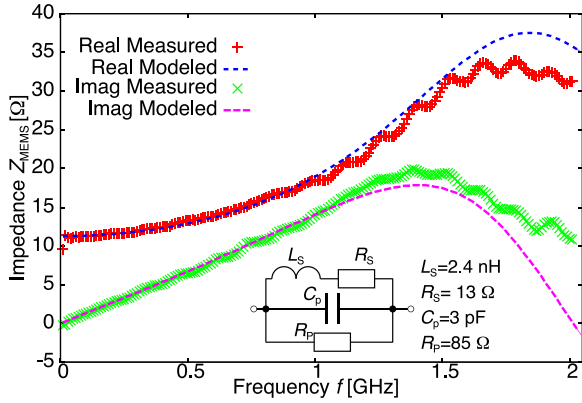


Fig. 18. RF impedance of the resistive microactuator.

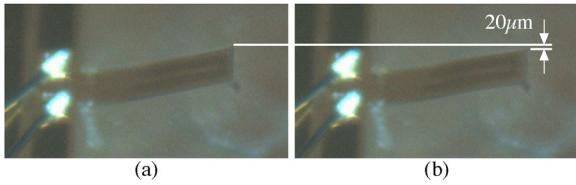


Fig. 19. (a) Initial state. (b) Head of thermal actuator goes down with 1 GHz RF wave.

20 μm in width and 0.1 μm in thickness [36]. The length and width of the actuator was 500 μm × 100 μm. Beneath the cantilever, aluminum was placed as a sacrificial layer and the cantilever curled up by 40 μm after the sacrificial layer etching. The resistance and inductance of the actuator were identified through the one-port measurement of the reverse scattering matrix  $S_{11}$  and by converting it into impedance using the following equation:

$$Z_{MEMS} = \frac{1 + S_{11}}{1 - S_{11}} Z_0 - 2R_{wire} - j2\omega L_{wire}, \quad (23)$$

where  $R_{wire}$  and  $L_{wire}$  refer to the resistance and inductance, respectively, of a 2 mm-long bonding wire. Their values had previously been identified by short measurements (i.e.,  $Z_{MEMS} = 0$ ) to be  $R_{wire} = 0.18 \Omega$  and  $L_{wire} = 2.1 \text{ nH}$ . Fig. 18 shows the real and imaginary parts of  $Z_{MEMS}$  and the equivalent circuit. The resistance and series inductance of the microactuator were identified as  $R_s = 13 \Omega$  and  $L_s = 2.4 \text{ nH}$ , respectively. As parasitics, a parallel capacitance of 3 pF and a current-limiting parallel resistance  $R_p = 85 \Omega$  were identified; these parasitics were not dominant at the frequency (1 GHz) of the following experiment ( $\therefore R_s \approx Z_L = 15 \Omega \ll Z_C = 53 \Omega < Z_p$ ).

The transmitter LC circuit was driven by an RF power source (Keysight Technologies, N9310A). The coils were placed at a distance of 90 μm. By applying the RF wave of 44.7 mW at 1 GHz to the first port (Tx circuit), the thermal actuator connected to the second port (Rx circuit) was heated up and the head of the microactuator was moved. As soon as the carrier wave was cut, the head of the actuator recovered its initial shape, as shown in Fig. 19. The movement distance was measured to be 20 μm, by a microscope. The equivalent applied power to the actuator was estimated by directly powering the actuator using DC: The current that

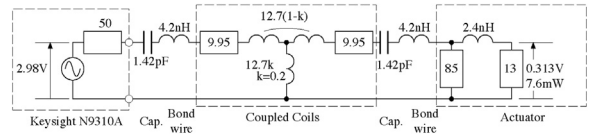


Fig. 20. Equivalent circuit of thermal actuator RF actuation experiment.

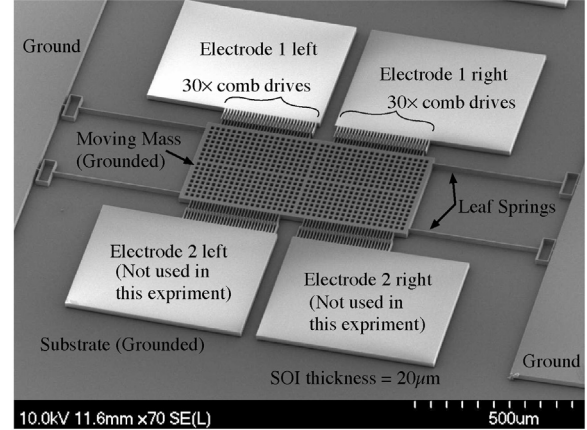


Fig. 21. Silicon MEMS resonator with  $f_M = 3.26 \text{ kHz}$ .

introduced the same amount of actuator movement (i.e., down by 20 μm) was estimated as the equivalent transferred power. The current was measured to be 25 mA and the power was measured to be 7.05 mW. Therefore, the power transfer efficiency was 15.8%. Fig. 20 is a complete equivalent circuit of the thermal actuator RF actuation experiment. In a linear circuit analysis using Berkeley Spice version 3f5 (AC analysis), the thermal actuator resistance had a maximum voltage of 0.313 V at 1 GHz, confirming approximately 7 mW of energy consumption at the actuator (7.6 mW in the calculation).

### 5. Capacitive microactuator mechanical resonance operation with AM carrier

As shown in Fig. 21, a silicon in-plane vibrating MEMS resonator was fabricated with a standard one-mask deep RIE process on a 2 cm-square SOI chip having 20 μm, 2 μm, and 627 μm device layer, SiO<sub>2</sub> sacrificial layer, and handling layer, respectively. It had a 748 μm × 348 μm mass structure with 3 μm-wide, 5 μm-pitch 60-teeth comb drive actuators on each side. On the structure, there were 40 × 16 holes of 12 μm × 8 μm for vapor hydrofluoric acid (VHF) dry release of the MEMS. The structure was suspended by four 4 μm × 480 μm silicon leaf springs, at the four corners. At the end of the spring there was a 44 μm × 100 μm hollow rectangular structure to relieve the tensile stress induced by movement. All these values were designed values. Because of the undercut in the first etching cycle of the deep RIE, the realized structure was thinner than the designed values. The undercut is nominally 0.3 μm from each side. The mechanical resonant frequency of the MEMS was approximately  $f_M = 3.26 \text{ kHz}$ . The resonator is commonly used as a typical MEMS design in experimental courses in the authors' institute and is known to produce mechanical amplification by a factor of ten at the resonant frequency [37].

The MEMS and coil chip were attached to two sides of an FR-4 glass epoxy PCB and were wire-bonded to a copper line to create a parallel resonant circuit for the energy receiver (Rx). A coaxial connector was attached at the end of the board to measure the impedance of the receiver circuit. The energy transmitter (Tx) was the same one used in the previous sections, with elec-

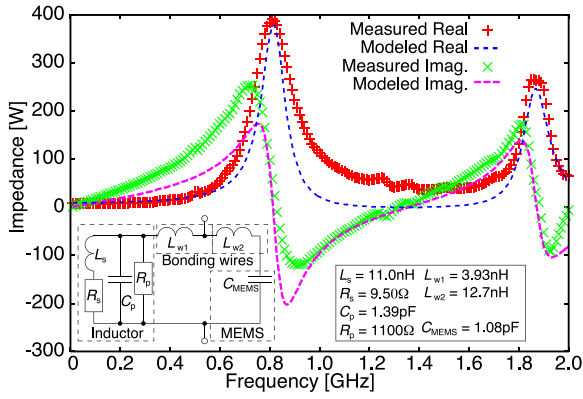


Fig. 22. Impedance of MEMS-coil energy receiver circuit and its equivalent model.

trical resonant frequency around 1.08 GHz. Prior to the actuation experiment, the frequency response was evaluated using a VNA, in the frequency range of 10 MHz to 2 GHz. Two resonant frequencies were observed: 827.0 MHz and 1.883 GHz. The impedance was modeled as shown in Fig. 22. The inductances of the bonding wires were added in between the MEMS capacitor and the inductor. The values were initially taken from individual measurements described before, and then identified by manual coarse search and least-squares fitting using the GNUplot graphing tool. In the results, all intrinsic values of coil inductance  $L_s$  (12.7–11.0 nH), its series resistance  $R_s$  (9.5  $\Omega$ ), bonding wire inductance to the coil  $L_{w1}$  (4.2–3.93 nH), and MEMS capacitor  $C_{MEMS}$  (1.4–1.08 pF) stayed in the same order of magnitude. Although the parasitic parallel capacitance  $C_p$  (57 fF to 1.39 pF) and bonding inductance to MEMS actuator  $L_{w2}$  (4.2–12.7 nH) were larger than the previously modeled values, and the limiting parallel resistance of the coil  $R_p$  (4900–1100  $\Omega$ ) decreased from the fitting result of individual measurement, their values stayed within the same orders of magnitude and the changes could be attributed to the environmental conditions such as longer bondwires and parasitic capacitances from the adjacent metal components. The remaining discrepancies could be decreased by adding more components such as a series resistance; further data may lead this article out of scope.

The entire view of the measurement setup is shown in Fig. 23. A sinusoidal driving signal  $f_m$  for MEMS was fed from the microsystem analyzer (Polytec MSA-500, Planar Motion Analyzer version 2.6) to the amplitude modulator of the RF generator N9310A. The RF-modulated output was fed to the MEMS under synchronous stroboscope microscope surveillance. The video images of the moving comb-drive teeth were analyzed using the built-in image recognition software of MSA-500, and the Bode diagram was obtained. The resonance of the MEMS used in the experiment could be expressed by a simple spring-mass-damper differential equation [37]:

$$m \frac{d^2x}{dt^2} + c \frac{dx}{dt} + kx = F \sin \omega t, \quad (24)$$

where  $m$ ,  $c$ ,  $k$ ,  $F$ ,  $\omega$ , and  $t$  are the representative mass, damping, spring constant, applied force, and angular frequency, respectively, of the sinusoidal wave ( $\omega = 2\pi f$ ). The solution derived from Eq. (24) is as follows:

$$x = \frac{x_{st}}{\sqrt{(1 - \kappa^2)^2 + (2\kappa\zeta)^2}} \sin(\omega t + \beta), \quad (25)$$

$$x_{st} = \frac{F}{k}, \quad (26)$$

$$\omega_M = \sqrt{\frac{k}{m}} = 2\pi f_M, \quad (27)$$

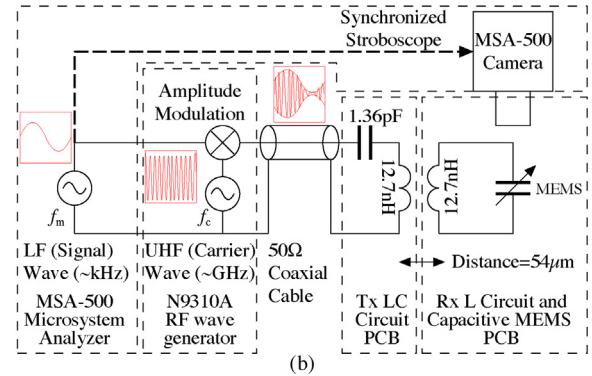
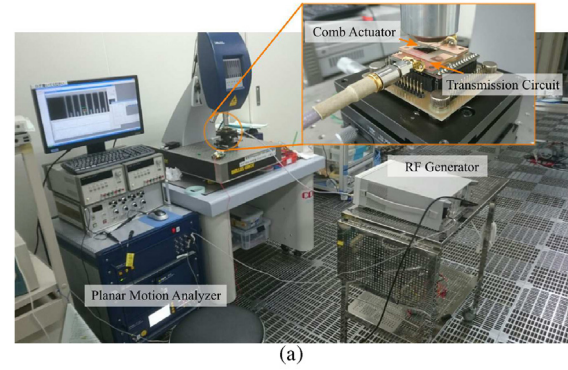


Fig. 23. (a) Photograph of experimental setup and (b) schematic diagram of the experimental system.

$$\beta = -\tan^{-1} \frac{2\kappa\zeta}{1 - \kappa^2}, \quad (28)$$

$$\kappa = \frac{\omega}{\omega_M}, \quad (29)$$

$$\zeta = \frac{c}{c_0}, \quad (30)$$

$$c_0 = 2\sqrt{mk}, \quad (31)$$

where  $x_{st}$ ,  $\beta$ ,  $\kappa$ ,  $\omega_M$ ,  $\zeta$ , and  $c_0$  are the static displacement, phase delay, relative applied frequency, intrinsic mechanical resonant angular frequency of MEMS, relative loss factor, and intrinsic stored energy, respectively.

Three configurations were tested: (a) AM RF signal was directly fed to MEMS. (b) AM RF signal was fed to receiver through inductive coupling; the series capacitor at the transmitter side (Fig. 23) was omitted. (c) AM signal was fed to the receiver through resonance coupling; Tx circuit was a series LC resonant circuit with  $C_s = 1.36$  pF. The measured Bode amplitude results were analyzed<sup>8</sup> through least-squares fitting with Eq. (25). The carrier frequency  $f_c$  was 750 MHz and its output power for  $Z_0 = 50 \Omega$  was set to 96.8 mW. The amplitude of the baseband signal (at  $f_m$ ) was set to 0.5 V (zero-peak) and the modulation rate was set to be 100%. The distance between coils was 54  $\mu\text{m}$ . As shown in Fig. 24, the AM RF signal carrier could drive the MEMS, by using the MEMS device itself as a rectifier. Eq. (25) could express well the mechanical resonance behavior. The static displacement  $x_{st}$ , i.e., movement obtainable while the MEMS was not in mechanical resonance, was found to be (a) 2.0 nm, (b) 2.2 nm, and (c) 2.86 nm. It should be noted that the maximum amplitude at resonance is approximately given by  $x_{st}/2\zeta$  ( $\zeta = 0.012 \ll 1$ ), yielding (a) 83 nm, (b) 92 nm, and (c) 119 nm. The analysis result confirmed an important finding described in Section

<sup>8</sup> Phases were also analyzed and coherent results were obtained.

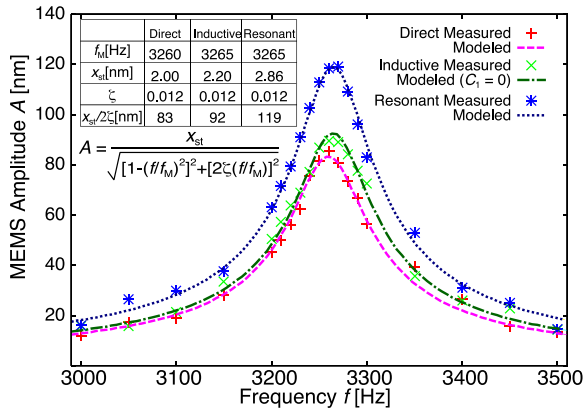


**Fig. 24.** Bode amplitude diagram of MEMS mechanical resonator remote driving. Label “Direct” refers to the case in which AM signal was directly fed to MEMS. Label “Inductive”: Power was sent to inductive coupling but series capacitance in the Tx circuit was omitted (short-circuited). Label “Resonant”: AM signal transfer by resonance.

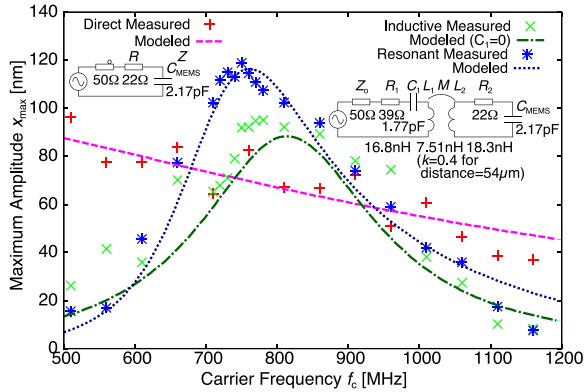


**Fig. 25.** Maximum amplitude dependency on carrier frequency  $f_c$ . Measurement results were analyzed with equivalent models.

2: “The LC resonant power transfer can produce a larger movement compared to the direct connection”. Such a scheme is extremely interesting because a MEMS driving circuit can work at a low voltage, and the voltage amplification is done in the MEMS chip (not in the LSI driver chip), thereby, validating the idea of separating the MEMS chip from the resonating receiver (Rx) and the LSI power transmitter (Tx).

Fig. 25 summarizes the peak amplitude dependence on carrier frequency  $f_c$ . Despite  $\pm 10$  nm of random fluctuations due to the limited magnification and recognition error of in-plane measurement of MSA-500, a model-based analysis could express the general tendency. The maximum amplitude  $x_{max}$  was proportional to the static displacement  $x_{st}$ , which was proportional to the applied force  $F$  (by Eq. (26)). The applied force was proportional to the square of the voltage across the capacitive MEMS  $V_{MEMS}$ . The above discussion can quantitatively be expressed by the following equations, by introducing an overall conversion factor  $\alpha$ :

$$x_{max} = \alpha V_{MEMS} V_{MEMS}^* \tag{32}$$

where  $V_{MEMS}^*$  denotes a complex conjugate number.

For calculating  $V_{MEMS}$ , the simplest models were adopted. In the case of (a) direct connection, a series resistance  $R$  was considered.  $V_{MEMS}$  and  $x_{max}$  were given by the following equations:

$$V_{MEMS} = \frac{V_o}{1 + j\omega C_{MEMS}(Z_o + R)} \tag{33}$$

$$x_{max} = \alpha V_{MEMS} V_{MEMS}^* = \frac{\alpha V_o^2}{1 + \omega^2 C_{MEMS}^2 (Z_o + R)^2} \tag{34}$$

where  $V_o$ ,  $Z_o$ , and  $C_{MEMS}$  are the effective output voltage at the source, output impedance of the source, and capacitance of MEMS, respectively. The maximum amplitude of cases (b) and (c) could also be modeled by using Eq. (32).  $V_{MEMS}$  was given by Eq. (14) with the simplest equivalent model described in Section 2.

Initial values were taken from the individual measurements such as from a coupled inductor energy transfer analysis (Fig. 16), and were least-squares fit using the measurement data. First, the (a) direct connection case was analyzed. The obtained conversion factor  $\alpha V_o^2 = 109$  nm and effective MEMS capacitance  $C_{MEMS} = 2.17$  pF were used for the following analyses. Then, the case (c) resonant transfer was fit through  $L_1$ ,  $L_2$ ,  $R_1$ , and  $C_1$ . The coupling coefficient  $k$  was set to 0.4 because the distance was shorter than that of the previous experiment ( $54 \mu\text{m}$  instead of  $k = 0.34$  for  $65 \mu\text{m}$ ). It turned out that the combination of  $L_1$  and  $L_2$  could minimize the error of either of the (b) or (c) measurements: to optimize case (b)  $(L_1, L_2) = (11.6, 18.1)$  [nH] and case (c)  $(L_1, L_2) = (25.8, 18.4)$  [nH]. By taking  $L_1$  from the value obtained from the power transfer measurement in the last section (Fig. 16), an effective combination of inductances was identified as:  $(L_1, L_2) = (16.8, 18.3)$  [nH]. As shown in Fig. 25, the modeled lines and measurement lines agree well, thereby validating the equivalent model analysis. The analysis also suggested the existence of a maximum efficiency frequency, which was approximately 750 MHz in the case of the authors’ experiment.

## 6. Conclusions

A concept to remotely feed actuation power to MEMS actuators using a UHF RF wave was proposed. This article theoretically derived and experimentally demonstrated that such actuation was possible by coupling MEMS-sized small inductances and configuring them in an LCR series resonance. The planar spiral coil of  $520 \mu\text{m} \times 520 \mu\text{m}$ , which was the same order in size as the typical MEMS devices was measured to have an inductance of approximately 10 nH and a self resonant frequency above 5 GHz. Using a pair of the coils, within the configuration of coupled series LCR resonant circuit, a 55.6% power efficiency was demonstrated for the load impedance  $Z_o = 50 \Omega$ , which was 8.29 times as large as that of simple induction coupling, i.e., without series capacitor. The coupling coefficient was identified to be  $k = 0.34$  for a distance of  $65 \mu\text{m}$ . Using the devices, two major types of MEMS actuators were driven remotely. One was a thermally actuated ciliary motion actuator, which appeared as approximately  $13 \Omega$  of resistance in an equivalent circuit. Remote power of 7.05 mW was consumed by the thermal actuator to provide  $20 \mu\text{m}$  of movement, for a 1 GHz 44.7 mW carrier wave input. The mode of operation was OOK; the actuator moved as long as the carrier wave was fed to the MEMS through the inductors. The other was a standard electrostatic comb-drive actuator integrated to a MEMS resonating structure of  $f_m = 3.26$  kHz. The 750 MHz 96.8 mW sinusoidal carrier wave was amplitude-modulated with 0.5 V sinusoidal low-frequency signal and was fed to the actuator. Approximately  $\pm 120$  nm of sinusoidal movement was observed using a stroboscopic microscope. The movement analysis showed that it was possible to provoke analog (not on–off) operation with the AM wave. Three configurations were compared and it was experimentally and theoretically proven that the resonant circuit could introduce a voltage amplification when compared to inductive coupling and direct connection of the AM wave to the MEMS device. All the circuits in the experiments could be analyzed as lumped parameter systems. The last important message of this article is that both thermal and electrostatic actuators work using the square of input–current for thermal and voltage for electrostatic actuator—and therefore, *it is the MEMS itself*

that rectifies the energy by simply connecting LC components. This fact systematically ensures the highest power efficiency when compared to any other existing method that uses additional rectifying components such as diodes. High power efficiency is an extremely interesting feature for power-aware system design. Future research direction may include integrated transmitter circuit research for MEMS operation and deployment in remote MEMS powering. The power-aware system design methodology presented in this article may open a door toward autonomous distributed sensors and actuator systems for the future.

## Acknowledgments

This project was partially supported by JSPS Kakenhi Grants-in-Aids (23686053 and 16H04345), and French national research grants (ANR-2011-BS03-005 and ANR-16-CE33-0022). CAD software for the layout design, MEMS process in the MEXT Nanotechnology Platform open facilities at the Takeda Sentanchi Supercleanroom were used through the VLSI Design and Education Center (VDEC), The University of Tokyo. We thank all members of the nanotechnology platform UTokyo VDEC for their invaluable assistances. Dr. Yasuyuki Ozeki of UTokyo is acknowledged for theoretical discussions.

## References

- [1] H. Fujita, Future of actuators and microsystems, *Sens. Actuators A: Phys.* 56 (1) (1996) 105–111, [http://dx.doi.org/10.1016/0924-4247\(96\)01282-4](http://dx.doi.org/10.1016/0924-4247(96)01282-4).
- [2] M. Ataka, A. Omodaka, N. Takeshima, H. Fujita, Fabrication and operation of polyimide bimorph actuators for a ciliary motion system, *J. Microelectromech. Syst.* 2 (4) (1993) 146–150, <http://dx.doi.org/10.1109/84.273089>.
- [3] S. Konishi, H. Fujita, A conveyance system using air flow based on the concept of distributed micro motion systems, *J. Microelectromech. Syst.* 3 (2) (1994) 54–58, <http://dx.doi.org/10.1109/84.294321>.
- [4] Y. Fukuta, Y.-A. Chapuis, Y. Mita, H. Fujita, Design, fabrication, and control of MEMS-based actuator arrays for air-flow distributed micromanipulation, *J. Microelectromech. Syst.* 15 (4) (2006) 912–926, <http://dx.doi.org/10.1109/JMEMS.2006.879378>.
- [5] Y. Mita, D. Collard, M. Mita, H. Fujita, Fabrication of an inverted scratch-drive-actuator for a powerful and precise conveyance system, *IEEJ Trans. Sens. Micromach.* 119 (12) (1999) 648–649, <http://dx.doi.org/10.1541/ieejsmas.119.648>.
- [6] T. Ebeffors, J.U. Mattsson, E. Kälvesten, G. Stemme, A robust micro conveyor realized by arrayed polyimide joint actuators, *J. Microchem. Microeng.* 10 (3) (2000) 337, <http://dx.doi.org/10.1088/0960-1317/10/3/307>.
- [7] S. Hollar, A. Flynn, S. Bergbreiter, K.S.J. Pister, Robot leg motion in a planarized-SOI, two-layer poly-Si process, *J. Microelectromech. Syst.* 14 (4) (2005) 725–740, <http://dx.doi.org/10.1109/JMEMS.2005.850720>.
- [8] K. Saito, K. Okazaki, T. Ogiwara, M. Takato, K. Saeki, Y. Sekine, F. Uchikoba, Locomotion control of MEMS microrobot using pulse-type hardware neural networks, *Electr. Eng. Jpn.* 186 (3) (2014) 43–50, <http://dx.doi.org/10.1002/ej.22473>.
- [9] N. Miki, I. Shimoyama, Soft-magnetic rotational microwings in an alternating magnetic field applicable to microflight mechanisms, *J. Microelectromech. Syst.* 12 (2) (2003) 221–227, <http://dx.doi.org/10.1109/JMEMS.2003.809966>.
- [10] Y. Uno, H. Qiu, T. Sai, S. Iguchi, Y. Mizutani, T. Hoshi, Y. Kawahara, Y. Kakehi, M. Takamiya, Luciola: a millimeter-scale light-emitting particle moving in mid-air based on acoustic levitation and wireless powering, *Proc. ACM Interact. Mob. Wearable Ubiquitous Technol.* 1 (4) (2017) 166, <http://dx.doi.org/10.1145/3161182>.
- [11] S.K. Chung, K. Ryu, S.K. Cho, A surface-tension-driven propulsion and rotation principle for water-floating mini/micro robots, 2009 IEEE 22nd International Conference on Micro Electro Mechanical Systems (2009) 1083–1086, <http://dx.doi.org/10.1109/MEMS.2009.4805575>.
- [12] Y. Mita, Y. Li, M. Kubota, S. Morishita, W. Parkes, L.I. Haworth, B.W. Flynn, J.G. Terry, T.-B. Tang, A.D. Ruthven, S. Smith, A.J. Walton, Demonstration of a wireless driven MEMS pond skater that uses EWOD technology Papers Selected from the 38th European Solid-State Device Research Conference 08, *Solid-State Electron* 53 (7) (2009) 798–802, <http://dx.doi.org/10.1016/j.sse.2009.02.020>.
- [13] N. Sakamoto, A. Frappé, B. Stefanelli, A. Kaiser, Y. Mita, Wireless drive of a MEMS ciliary motion actuator via coupled magnetic resonances using micro inductors, 2015 18th International Conference on Solid-State Sensors, Actuators and Microsystems (TRANSDUCERS) (2015) 1961–1964, <http://dx.doi.org/10.1109/TRANSDUCERS.2015.7181337>.
- [14] S. Takeuchi, N. Futai, I. Shimoyama, Selective drive of electrostatic actuators using remote inductive powering, *Technical Digest. MEMS 2001. 14th IEEE International Conference on Micro Electro Mechanical Systems (Cat. No. 01CH37090)* (2001) 574–577, <http://dx.doi.org/10.1109/MEMSYS.2001.906606>.
- [15] S. Takeuchi, I. Shimoyama, Selective drive of electrostatic actuators using remote inductive powering, *Sens. Actuators A: Phys.* 95 (2–3) (2002) 269–273, [http://dx.doi.org/10.1016/S0924-4247\(01\)00738-5](http://dx.doi.org/10.1016/S0924-4247(01)00738-5).
- [16] S.H. Byun, J. Yuan, M.G. Yoon, S.K. Cho, Wirelessly powered electrowetting-on-dielectric (EWOD) by planar receiver coils, *J. Microchem. Microeng.* 25 (3) (2015) 035019, URL <http://stacks.iop.org/0960-1317/25/i=3/a=035019>.
- [17] P. Basset, A. Kaiser, B. Legrand, D. Collard, L. Buchailot, Complete system for wireless powering and remote control of electrostatic actuators by inductive coupling, *IEEE/ASME Trans. Mechatron.* 12 (1) (2007) 23–31, <http://dx.doi.org/10.1109/TMECH.2006.886245>.
- [18] T. Sekitani, M. Takamiya, Y. Noguchi, S. Nakano, Y. Kato, T. Sakurai, T. Someya, A large-area wireless power-transmission sheet using printed organic transistors and plastic MEMS switches, *Nat. Mater.* 6 (2007) 413–417, <http://dx.doi.org/10.1038/nmat1903>.
- [19] M. Takamiya, T. Sekitani, Y. Miyamoto, Y. Noguchi, H. Kawaguchi, T. Someya, T. Sakurai, Design solutions for a multi-object wireless power transmission sheet based on plastic switches, 2007 IEEE International Solid-State Circuits Conference, *Digest of Technical Papers* (2007) 362–609, <http://dx.doi.org/10.1109/ISSCC.2007.373444>.
- [20] H. Fuketa, K. Yoshioka, T. Yokota, W. Yukita, M. Koizumi, M. Sekino, T. Sekitani, M. Takamiya, T. Someya, T. Sakurai, 30.3 organic-transistor-based 2 kV ESD-tolerant flexible wet sensor sheet for biomedical applications with wireless power and data transmission using 13.56 MHz magnetic resonance, 2014 IEEE International Solid-State Circuits Conference *Digest of Technical Papers (ISSCC)* (2014) 490–491, <http://dx.doi.org/10.1109/ISSCC.2014.6757525>.
- [21] A.N. Laskovski, M.R. Yuce, Class-E self-oscillation for the transmission of wireless power to implants, *Sens. Actuators A: Phys.* 171 (2) (2011) 391–397, <http://dx.doi.org/10.1016/j.sna.2011.07.018>.
- [22] A.N. Laskovski, T. Dissanayake, M.R. Yuce, Stacked spirals for biosensor telemetry, *IEEE Sens. J.* 11 (6) (2011) 1484–1490, <http://dx.doi.org/10.1109/JSEN.2010.2091123>.
- [23] M.S. Mohamed Ali, K. Takahata, Frequency-controlled wireless shape-memory-alloy microactuators integrated using an electroplating bonding process, *Sens. Actuators A: Phys.* 163 (1) (2010) 363–372, <http://dx.doi.org/10.1016/j.sna.2010.08.007>.
- [24] P. Li, T.K. Givrad, D.P. Holschneider, J.-M.I. Maarek, E. Meng, A. Parylene MEMS electrothermal valve, *J. Microelectromech. Syst.* 18 (6) (2009) 1184–1197, <http://dx.doi.org/10.1109/JMEMS.2009.2031689>.
- [25] M.S.M. Ali, B. Bycraft, A. Bsoul, K. Takahata, Radio-controlled microactuator based on shape-memory-alloy spiral-coil inductor, *J. Microelectromech. Syst.* 22 (2) (2013) 331–338, <http://dx.doi.org/10.1109/JMEMS.2012.2221161>.
- [26] J. Fong, Z. Xiao, K. Takahata, Micromachined rectangular-spiral-coil actuator for radio-controlled cantilever-like actuation, *Sens. Actuators A: Phys.* 226 (2015) 107–115, <http://dx.doi.org/10.1016/j.sna.2015.02.024>.
- [27] P.S. Chee, M.N. Minjal, P.L. Leow, M.S.M. Ali, Wireless powered thermo-pneumatic micropump using frequency-controlled heater, *Sens. Actuators A: Phys.* 233 (2015) 1–8, <http://dx.doi.org/10.1016/j.sna.2015.06.017>.
- [28] T. Imura, H. Okabe, Y. Hori, Basic experimental study on helical antennas of wireless power transfer for electric vehicles by using magnetic resonant couplings, 2009 IEEE Vehicle Power and Propulsion Conference (2009) 936–940, <http://dx.doi.org/10.1109/VPPC.2009.5289747>.
- [29] A. Kurs, A. Karalis, R. Moffatt, J.D. Joannopoulos, P. Fisher, M. Soljačić, Wireless power transfer via strongly coupled magnetic resonances, *Science* 317 (5834) (2007) 83–86, <http://dx.doi.org/10.1126/science.1143254>.
- [30] K. Kurokawa, Power waves and the scattering matrix, *IEEE Trans. Microw. Theory Tech.* 13 (2) (1965) 194–202, <http://dx.doi.org/10.1109/TMTT.1965.1125964>.
- [31] K.-Y. Lee, S. Mohammadi, P.K. Bhattacharya, L.P.B. Katehi, Wideband compact model for integrated inductors, *IEEE Microw. Wirel. Compon. Lett.* 16 (9) (2006) 490–492, <http://dx.doi.org/10.1109/LMWC.2006.880712>.
- [32] K.-Y. Lee, S. Mohammadi, P.K. Bhattacharya, L.P.B. Katehi, Compact models based on transmission-line concept for integrated capacitors and inductors, *IEEE Trans. Microw. Theory Tech.* 54 (12) (2006) 4141–4148, <http://dx.doi.org/10.1109/TMTT.2006.886157>.
- [33] C. Neagu, C. Rusu, H. Jansen, A. Smith, J. Gardeniers, M. Elwenspoek, Characterization of a planar microcoil for implantable microsystems, *Sens. Actuators A: Phys.* 62 (1) (1997) 599–611, [http://dx.doi.org/10.1016/S0924-4247\(97\)01601-4](http://dx.doi.org/10.1016/S0924-4247(97)01601-4).
- [34] S.S. Mohan, M. del, M. Hershenson, S.P. Boyd, T.H. Lee, Simple accurate expressions for planar spiral inductances, *IEEE J. Solid-State Circuits* 34 (10) (1999) 1419–1424, <http://dx.doi.org/10.1109/4.792620>.
- [35] H.A. Wheeler, Simple inductance formulas for radio coils, *Proc. IRE* 16 (10) (1928) 1398–1400, <http://dx.doi.org/10.1109/JRPROC.1928.221309>.
- [36] J. Malapert, S. Morishita, M. Ataka, H. Fujita, D. Collard, Y. Mita, Power regulated thermal actuator based on UV-patterned polyimides for ciliary motion system, *IEEJ Trans. Sens. Micromach.* 133 (3) (2013) 77–84, <http://dx.doi.org/10.1541/ieejsmas.133.77>.
- [37] Y. Mita, A. Hirakawa, B. Stefanelli, I. Mori, Y. Okamoto, S. Morishita, M. Kubota, E. Lebrasseur, A. Kaiser, Progress and opportunities in high voltage microactuator powering technology towards one-chip MEMS, *Jpn. J. Appl. Phys.* 57 (2018) 04FA05, <http://dx.doi.org/10.7567/JJAP.57.04FA05>.

## Biographies

**Yoshio Mita** is an associate professor of the Department of Electrical Engineering and Information Systems, the University of Tokyo. He got his Bachelor, Master, and Ph.D. degrees of Electrical Engineering from the University of Tokyo in 1995, 1997 and 2000, respectively. After Ph.D., he was appointed as an assistant professor of VLSI Design and Education Center (VDEC), and was promoted to Lecturer at the Department of Electrical Engineering in 2001 and then to Associate Professor in 2005. Since 2012, Dr. Mita serves as the MEXT Nanotechnology Platform UTokyo Nanofabrication site manager. His research interest includes VLSI integrated MEMS.

**Naoyuki Sakamoto** received B.E. and M.E. degrees in electrical engineering from the University of Tokyo in 2013 and 2016 respectively. From 2013 to 2016 he served also as an assistant technician of the University of Tokyo for VDEC Nanotechnology Platform. His M.S. degree dissertation deals with wireless resonant power transfer. Since 2016 he is working in Yamaha Corporation.

**Naoto Usami** received his B.E., M.E. degrees in electrical engineering from The University of Tokyo, in 2014 and 2016, respectively. He is currently working toward the Ph.D. degree at the Department of Electrical Engineering and Information Systems, The University of Tokyo. In 2014, he had been serving as a sub project manager for realization of Deep Space Sculpture “DESPATCH” which was a part of Artsat project. His current interest includes antenna design, micro remote powering, Synthetic Aperture Radar (SAR), micro and nano fabrication, and reconfigurable autonomous distributed microsystems.

**Antoine Frappé** received the M.S. and Ph.D. degrees in electrical engineering from the Université des Sciences et Technologies de Lille, in 2004 and 2007. He also graduated from the Institut Supérieur d'Electronique et du Numérique (I.S.E.N.) engineering school in Lille in 2004. In 2007, he was with the Silicon Microelectronics group at the Institut d'Electronique, de Microelectronique et des Nanotechnologies (I.E.M.N.) in Lille. He received a Fulbright grant in 2008 to pursue research in communication systems at the Berkeley Wireless Research Center at UC Berkeley, CA. He is now an Associate Professor at I.S.E.N. and leads the Integrated Circuits Design group at I.E.M.N. His current research interests concern digital RF transmitters, software-defined radio and mixed-signal design for RF and mmW communication systems.

**Akio Higo** was born in Tokyo, Japan in 1977. He received the B.E. from Seikei University, Japan, in 2002 and the M.E. and the Ph.D. degrees from the University of Tokyo, Japan, in 2007. From 2007 to 2012, he was an Assistant Professor in Research Center for Advanced Science and Technology, the University of Tokyo. Since 2012 to 2017, he was an Assistant Professor in WPI-AIMR, Tohoku University. He is currently a project lecture in VLSI design and education research center, the University of Tokyo. His research interests include III–V/Si integrated photonic circuits, Optical MEMS, III–V nanophotonic devices and III–N devices. Dr. Higo is member of JSAP, IEEJ, IEICE, SPIE, OSA and IEEE. He was recipients of Young Scientist Award from the 10th International Conference on Optical Internet 2012.

**Bruno Stefanelli** received the engineering diploma from the Institut Supérieur d'Electronique du Nord (ISEN), Lille, France, in 1986. In 1992 he received the Ph.D. degree from the University of Lille. In 1992, he joined the analog/RF IC design group at the Institut d'Electronique, de Microelectronique et de Nanotechnologies (IEMN) in Villeneuve-d'Ascq where he worked on continuous and discrete time analog circuits, data-converters and RF-MEMS. His present research activities concern RF and millimeter wave circuits for telecommunications. He is also professor at ISEN.

**Hidehisa Shiomi** is an assistant professor of Osaka University. He has got his Ph.D. from Tokai University on March 2000. Since April 2000 he is appointed as an assistant professor of Osaka University. His research interests include microwave, electrical circuit, adaptive control, microwave antenna and simulations.

**Julien Bourgeois** is a Professor of computer science with the University of Franche-Comté (UFC), Montbéliard, France. He is also part of the Franche Comté Electronique Mécanique Thermique et Optique-Sciences et Technologies (Femto-ST) Institute (UMR CNRS 6174), UFC, where he is leading the Complex Networks Team. He was an Invited Professor with Carnegie Mellon University, Pittsburgh, PA, USA, from September 2012 to August 2013; with Emory University, Atlanta, GA, USA, in 2011; and with The Hong Kong Polytechnic University, Hung Hom, Hong Kong, in 2010 and 2011. He is currently leading the topic of system architecture, communication, and networking with Laboratoire d'Excellence (LABEX) ACTION, which is a 10-M funded program that aims to build integrated smart systems. He collaborated with several other institutions (e.g., the Lawrence Livermore National Laboratory, the Oak Ridge National Laboratory, etc.). He has worked for more than ten years in his topics of interest, and he is the coauthor of more than 70 international publications and communications. Apart from his research activities, he is acting as a Consultant for the French government and for private companies. His research interests include distributed intelligent microelectromechanical systems (MEMS).

**Andreas Kaiser** received the engineering diploma from the Institut Supérieur d'Electronique du Nord (ISEN), Lille, France, in 1984, and the Ph.D. degree in 1990 from the University of Lille. In 1990 he joined the Centre National de la Recherche Scientifique (CNRS) where he was responsible for the analog/RF IC design group at the Institut d'Electronique, de Microelectronique et de Nanotechnologies (IEMN) in Lille. He is currently vice-president for research and innovation at the Yncrea engineering graduate school. His research interests are continuous and discrete time analog circuits, data-converters, analogue design automation, RF-MEMS and RF circuits. Prof. Kaiser served as TPC Chair of the European Solid State Circuits Conference in 1995 and 2005 and has been a guest and associate editor to the IEEE Journal of Solid State Circuits.